

Advanced electrically conductive carbon nanotubes-PVDF composite membranes with electro-promoted water treatment performance

Received: 29 April 2025

Accepted: 27 October 2025

Published online: 16 December 2025

 Check for updates

Yongke Zhang^{1,2}, Jiajian Xing^{1,2}, Gaoliang Wei^{1,2}, Linhua Rao¹, Guangze He¹, Hao Du¹, Haiguang Zhang¹, Xu Wang¹, Shuo Chen¹ & Xie Quan¹✉

Decentralized water supply is essential for providing clean and safe drinking water, especially in underdeveloped regions. Membrane technology is a key process for removing pathogens and suspended solids from polluted water sources. This study constructs electrically conductive membranes (ECMs) using carbon nanotubes (CNTs) confined within polarized poly(vinylidene fluoride) (PVDF) through C-F interactions. The resulting membranes achieve ultrahigh water permeance, 3.5 to 5.2 times higher than four commercial polymer membranes with similar pore sizes. They maintain good electrical conductivity and mechanical strength. Applying a weak negative potential induces electrostatic repulsion between the ECMs and foulants, enhancing antifouling performance by over 10 times in terms of backwashing interval compared to conventional polymer membranes. A demonstration project confirms the feasibility of industrial-scale production with a capacity of 11.5 m² h⁻¹, corresponding to an annual yield of approximately 100,000 m². Another field demonstration for drinking water treatment, with a capacity of 300 m³ day⁻¹, shows improved effluent quality, 53% energy savings, and 95% cost reduction for chemical cleaning compared to conventional processes. This study provides a cost-effective and efficient solution for addressing drinking water security challenges in underdeveloped regions through the enhanced performance of CNTs-PVDF ECMs.

Global population growth and severe climate change are compounding water scarcity in arid regions, while contamination from industrial effluents, agricultural runoff, and urban waste depletes safe water supplies^{1,2}. According to a new report from the United Nations (UN) World Water Development, around 3.6 billion people lack adequate sanitation services for accessing clean and safe drinking water. The sustainable development goals of clean water promoted by the UN aim to ensure availability and sustainable management of water and

sanitation for all by 2030³. The gap between current situation and goals mainly lies in the water security issues in underdeveloped areas, which lack centralized water treatment and distribution systems, or have nonexistent sanitation facilities. It is currently an important issue with an increasing demand for innovative water purification technologies to provide safe and clean water^{4,5}. As a physical strategy, membrane filtration is an effective technology to close the gap of water security demands in undeveloped areas, which could provide reliable

¹Key Laboratory of Industrial Ecology and Environmental Engineering (Ministry of Education, China), School of Environmental Science and Technology, Dalian University of Technology, Dalian, China. ²These authors contributed equally: Yongke Zhang, Jiajian Xing, Gaoliang Wei. ✉e-mail: quanxie@dlut.edu.cn

removal of pathogens, easy deployment and decentralized operation, low operational cost and maintenance^{5,6}, minimized or even eliminated chemical agents or disinfectants^{7,8}. However, current membranes still face serious challenges of low water permeance and persistent membrane fouling accumulation, restricting their wider applications in low-income countries or areas^{9–11}. Recently, electrically conductive membranes (ECMs) represent a revolutionary advancement over conventional membranes, which could combine electrochemistry to improve significantly water penetration, ions/molecules rejection, and antifouling performance^{12–14}. However, there is still a great challenge to fabricate the ECMs concurrently possessing high filtration performance, high electrical conductivity, and high mechanical strength at present. Overcoming the challenges requires innovative approaches in material design, processing methods, and a deep understanding of the interplay among electrical, mechanical, and filtration characteristics.

Among the materials for fabrication of the ECMs, carbon nanotubes (CNTs) have emerged as one of the preferred materials owing to their exceptional electrical conductivity (generally higher than $1 \times 10^4 \text{ S m}^{-1}$), and atomically smooth inner/outer surface¹⁵. Molecular dynamic simulations show that, in these atomically smooth and hydrophobic CNTs, water molecules exhibit a free-slip flow with rates 4–5 orders of magnitude higher than those calculated from Knudsen diffusion¹⁶. However, the membranes with separation layers composed entirely of CNTs are structurally fragile, making them difficult for practical application. It has been reported that CNTs could be integrated with polymers to significantly improve mechanical strength of CNTs membranes, which allows them to withstand higher pressures and harsh operating conditions without deforming or fracture^{12,17}.

Among these polymers, PVDF is widely adopted as a base polymer for fabricating membranes owing to its outstanding chemical inertness, excellent mechanical robustness, and favorable cost profile. Currently, some CNTs-PVDF composite membranes have been reported^{18–23}, most of which are structurally classified as flat-sheet membranes. Compared with the flat-sheet membranes, hollow fiber membranes usually offer clear advantages, including higher packing density, lower investment cost, and lower energy consumption. Recently, several studies have reported the CNTs-PVDF hollow fiber membranes^{24,25}, which were prepared by depositing CNTs on PVDF membrane substrate via vacuum-assisted filtration. Since PVDF merely acts as the substrate and the CNTs are not crosslinked, this membrane is structurally unstable and is far from practical applications. It is believed that the usage of PVDF to crosslink CNTs to construct a CNTs-PVDF hollow fiber membranes could resolve the problem. However, such membranes have been rarely reported. It is still a great challenge to fabricate such membranes with high performance, primarily due to the trade-off among their separation performance, structural stability, and electrical conductivity.

In this study, we propose a method for scalable fabrication of the CNTs-PVDF hollow fiber membranes with high separation performance, through the synergic regulation of well-designed wet-spinning parameters. Benefiting from the unspoiled smooth surface of CNTs, the membranes have a permeance of 3.5–5.2 times higher than those of commercial PVDF membranes with a similar pore size. More importantly, since β -phase PVDF has a net dipole moment per unit cell, and the fluorine atoms in the all-trans chain of β -phase PVDF are highly electronegative, the molecule chains could potentially function as “bridges” to lower the energy barrier for electron conductivity between adjacent CNTs via their interactions with π -bonds of CNTs, exhibiting a good electrical conductivity. We also report that a negative potential on the membranes could induce a dense water layer at water/CNTs interface and electrostatic repulsion between the membrane and negatively charged foulants (such as natural organic matter (NOM), microorganisms, oil-droplets, and clay colloids, etc.), which could inhibit the foulants from adhering onto the membranes, and

thus significantly improve their antifouling performance. A demonstration project for scalable fabrication of the CNTs-PVDF composite ECMs with a production rate of $11.5 \text{ m}^2 \text{ h}^{-1}$ (corresponding to an annual yield of around $100,000 \text{ m}^2$) has evidenced the feasibility of their industrial-scale production. Another field demonstration project for drinking water treatment with a capacity of $300 \text{ m}^3 \text{ day}^{-1}$ demonstrates that the electrified membrane process equipped with the ECMs produces water with much better quality and low operation cost, and saves about 53% energy consumption and 95% cost for chemical cleaning in comparison to conventional drinking water treatment process. This study presents a revolutionary approach for boosting performance of membrane technology, which may provide a cost-effective, easily manageable, and highly efficient approach to tackle the critical drinking water security challenges faced by people from underdeveloped regions.

Results and discussion

Membrane fabrication and characterization

The CNTs-PVDF hollow fiber membranes were fabricated through continuous wet-spinning of cast dispersion, which was prepared by dispersing the α -phase PVDF powder and pristine CNTs into organic solvent. The continuous wet-spinning process mainly includes the phase conversion in coagulation bath, water/hot water wash, soak in glycerol, and product collection (Supplementary Fig. 1). As schematically shown in Fig. 1a, the solidified membranes gradually exhibit an organized structure following the stages of gravity-driven traction, flow-driven traction, and drawing-driven traction due to the combined effects of shear flow and solvent exchange. The X-ray diffraction (XRD) and Fourier transform infrared (FTIR) spectra of PVDF powder and CNTs-PVDF dispersion demonstrate that the α -phase PVDF is partially converted to β -phase PVDF during the stirring process of the dispersion, for which the percentage of β -phase PVDF was increased from 30.19% to 38.12% (Supplementary Figs. 2–4 and Table 1). Since the β -phase PVDF is a polar crystalline form possessing a net dipole moment per unit cell caused by an all-trans (TTTT) conformation of PVDF molecular chains, the chains could interact with π -bonds of CNTs^{26,27}, which could diminish van der Waals interactions among CNTs and promote their uniform dispersion (Fig. 1b and Supplementary Figs. 5–7). The Raman spectra show the intensity ratio of G peak to D peak (I_G/I_D) for the cast dispersion is increased in comparison to that of raw CNTs powder (Supplementary Fig. 8), suggesting the graphitization of CNTs is improved during their dispersion process. The improved graphitization of CNTs should be attributed to the fact that the stir-induced shear forces lead to the detachment of sp^3 amorphous carbon from CNTs and an enhanced exposure of sp^2 hybridized carbon atoms, which is conducive to the increase of both water permeance and electrical conductivity.

The fabricated membranes are shown in Fig. 1c, verifying the feasibility of large-scale preparation of CNTs-PVDF membranes. Meanwhile, with the tensile force along the axial direction and the progression of phase conversion, the thickness of the separation layer were gradually decreased from 138 nm for CNTs-PVDF₃₀ membranes to 95 nm for CNTs-PVDF₁₀₀ membrane, which could lower the water transport resistance across the membranes separation layer. The scanning electron microscope (SEM) images of the fabricated CNTs-PVDF membranes are shown in Fig. 1d–f and Supplementary Figs. 9 and 10. Their surfaces exhibit a porous structure formed by the interlacement of CNTs and PVDF. The cross-sectional SEM images show that the CNTs-PVDF membranes feature a dense skin layer and highly porous inner surface. The thin dense layer could contribute to the selective passage of water molecules while rejecting contaminants. The distinctly porous inner surface is conducive to rapid water transport. It could be observed that the CNTs underneath the separation layer tend to be arrayed parallelly to water transport pathways (Fig. 1f, g), which is induced by shrinkage and agglomeration of PVDF chains

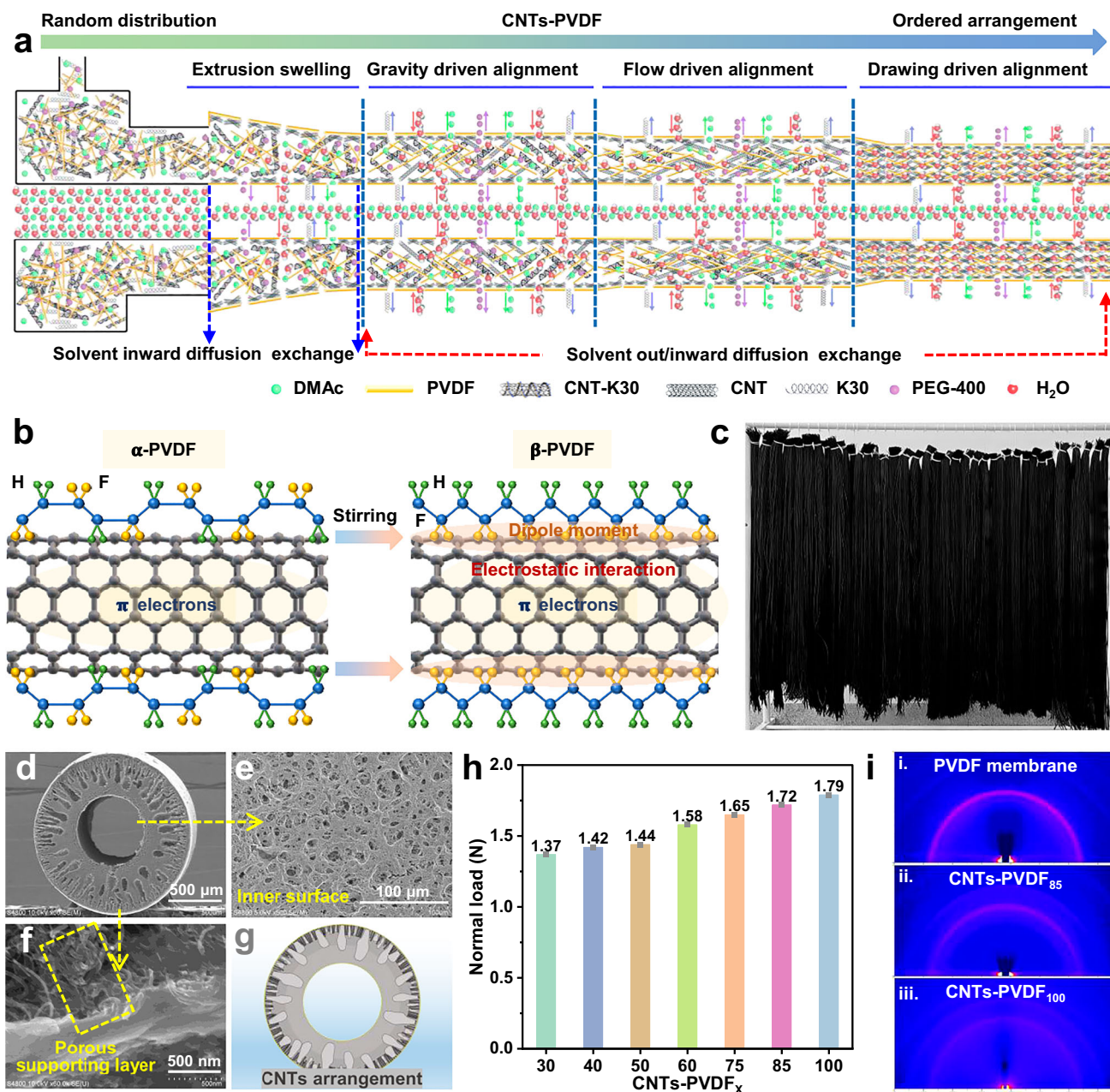


Fig. 1 | Wet-spinning preparation and characterization of CNTs-PVDF membranes. a Arrangement of CNTs during the membrane fabrication process from dispersion to membrane. **b** Interaction between CNTs and PVDF. **c** Fabricated CNTs-PVDF membrane at large-scale. **d–f** SEM images of cross-section, inner

surface, and supporting layer of CNTs-PVDF membrane. **g** Schematic illustration of cross-section of CNTs-PVDF membrane. **h** Breaking load forces of the CNTs-PVDF membranes. **i** 2D-WAXD pattern of the PVDF membrane, CNTs-PVDF₈₅ membranes and CNTs-PVDF₁₀₀ membrane.

during phase conversion because of the exchange between water and solvent. The aligned CNTs could provide short and direct pathways for water molecules to pass through the membrane, reducing hydraulic resistance and enhancing water permeance.

It is found that the extrusion velocity of cast dispersion is an important factor that affects structural strength and electrical conductivity of resultant CNTs-PVDF membranes. Seven CNTs-PVDF_x membranes were prepared by regulating extrusion velocity ($x = 30, 40, 50, 60, 75, 85, \text{ and } 100 \text{ mL h}^{-1}$). As shown in Supplementary Fig. 11, all CNTs-PVDF_x membranes (CNTs-PVDF₃₀, CNTs-PVDF₄₀, CNTs-PVDF₅₀, CNTs-PVDF₆₀, CNTs-PVDF₇₅, CNTs-PVDF₈₅, CNTs-PVDF₁₀₀) exhibit perfectly circular cross sections. With an increase in extrusion velocity from 30 to 100 mL h⁻¹, their outer diameters increase from 1.35 mm for CNTs-PVDF₃₀ membranes to 1.55 mm for CNTs-PVDF₁₀₀ membranes.

Tensile stress tests show the increased thickness improves the breaking load of the CNTs-PVDF membranes from 1.37 to 1.79 N (Fig. 1h and Supplementary Fig. 12). The breaking load of 1.79 N is comparable to those of commercial PVDF membranes (Supplementary Fig. 13), suggesting the mechanical strength of CNTs-PVDF membranes is sufficient for practical water treatment applications. Meanwhile, the SEM showed the low extrusion rate at 30 and 40 mL h⁻¹ would lead to asymmetric membrane wall due to the uneven surface tension at the spinneret^{28,29}. When the extrusion velocity during membrane fabrication was increased to 50–100 mL h⁻¹, the cross-section and surface of the CNTs-PVDF membranes were uniform and no visible defects of the CNTs-PVDF membranes were observed on industrial-scale, which confirmed their practicality (Supplementary Fig. 14). The increase of extrusion velocity could also enhance intensity of F1s peak in X-ray

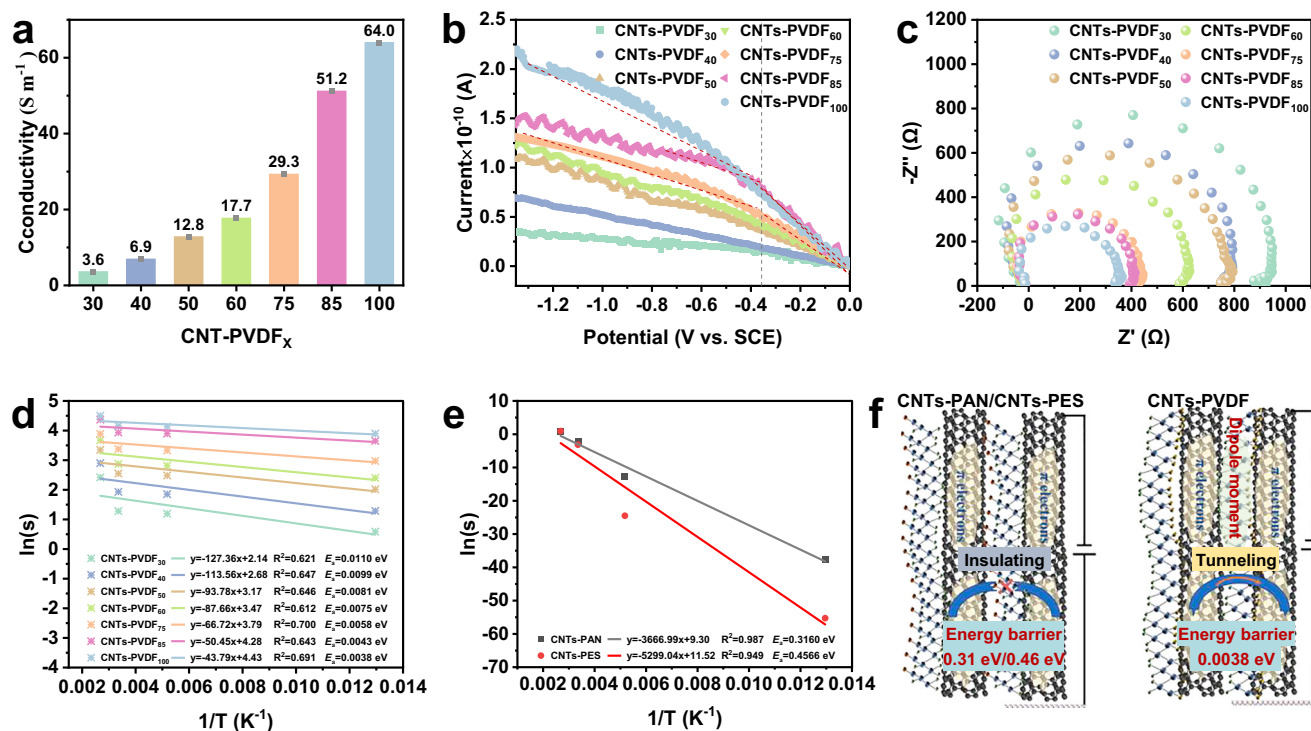


Fig. 2 | Characterization of electrical properties of CNTs-PVDF membrane.

a Electrical conductivity of CNTs-PVDF₃₀, CNTs-PVDF₄₀, CNTs-PVDF₅₀, CNTs-PVDF₆₀, CNTs-PVDF₇₅, CNTs-PVDF₈₅, and CNTs-PVDF₁₀₀. **b** $I-V$ curves of the CNTs-PVDF membranes. The dashed lines are guides to the eye. **c** Electrochemical impedance spectroscopy of the membranes. **d** The Arrhenius equation fitting of

conductivity variation with temperature of CNTs-PVDF membranes and calculated activation energy. **e** The Arrhenius equation fitting of conductivity variation with temperature of CNTs-PAN and CNTs-PES membranes and calculated activation energy. **f** Schematic diagram of electron tunneling effects.

photoelectron spectra (XPS) of corresponding CNTs-PVDF membranes, which indicates the promotion of polar β -phase PVDF (Supplementary Fig. 15)³⁰. The XRD spectra and FTIR analyses also suggested that the increase of extrusion velocity could promote conversion from α -phase PVDF to β -phase PVDF. When the extrusion velocity increases from 30 to 100 $mL\ h^{-1}$, the relative percentage of β -phase PVDF was linearly increased from 44.25% to 87.68% (Supplementary Figs. 16 and 17 and Table 2). The inference could be further confirmed by 2D wide-angle X-ray diffraction (2D-WAXD) patterns (Fig. 1i and Supplementary Fig. 18), in which a strong diffraction arc for CNTs-PVDF₃₀ membranes gradually changes over to a weak diffraction arc-spot for CNTs-PVDF₁₀₀ membranes with an increase of extrusion velocity from 30 to 100 $mL\ h^{-1}$, since diffraction arc and diffraction arc-spot are typical patterns of α -phase and β -phase PVDF, respectively^{31,32}.

The electrical conductivity of CNTs-PVDF membranes as a function of extrusion velocity is shown in Fig. 2a. With the increase of extrusion velocity from 30 to 40, 50, 60, 75, 85, and 100 $mL\ h^{-1}$, the electrical conductivity of dried CNTs-PVDF membranes increases from 3.6, to 6.9, 12.8, 17.7, 29.3, 51.2, and 64.0 $S\ m^{-1}$ respectively, which could be attributed to the increased relative percentage of β -phase PVDF from 44.25% to 87.68%. The electrical conductivity of CNTs-PVDF membrane is 9–11 orders of magnitude higher than that of PVDF membranes (10^{-10} – 10^{-9} $S\ m^{-1}$, Supplementary Fig. 19), verifying good electrical conductivity of CNT-PVDF membranes and the success in preparation of ECMs. To further demonstrate their high electrical conductivity, CNTs-polyacrylonitrile (CNTs-PAN) membranes and CNTs-poly(ether sulfone) (CNTs-PES) membranes were also prepared under the same conditions for comparison. It is found that the electrical conductivity (64.0 $S\ m^{-1}$) of CNTs-PVDF₁₀₀ membranes is 2–3 orders of magnitude higher than those of CNTs-PAN membranes (0.128 $S\ m^{-1}$) and CNTs-PES membranes (0.043 $S\ m^{-1}$, Supplementary Fig. 20), though they have the same mass ratio of CNTs to polymer.

Meanwhile, the comparison of the electrical conductivity among conductive composite membranes shows that the CNTs-PVDF₈₅ membrane exhibited an excellent conductivity of 51.2 $S\ m^{-1}$, which is significantly higher than those of other conductive CNTs-polymer composite membranes reported in previous studies (Supplementary Table 3).

To understand the unexpectedly high conductivity of CNTs-PVDF membranes, electrochemical tests were subsequently performed. As shown in Fig. 2b, their $I-V$ curves show a typical nonlinear behavior with the membrane potential between 0 and -0.35 V vs. Ag/AgCl, and the current gradually increased linearly with the potential increasing from -0.35 to -1.35 V vs. Ag/AgCl. This $I-V$ variation phenomenon could be attributed to the electron tunneling behavior motivated by an external electrical potential³³. Electrochemical impedance spectroscopy (EIS) curves were measured to analyze the electron transport resistance within the CNTs-PVDF membranes. The result shows that the Nyquist plots exhibit a significant reduction in charge transfer resistance for the CNTs-PVDF₁₀₀ membrane in comparison to CNTs-PVDF₃₀ membranes (Fig. 2c). Temperature-dependent conductivities were also measured and the activation energy (E_a) was calculated from Arrhenius equations to further assess the electron transport behavior (Fig. 2d, e). E_a stands for the minimum energy barrier that needs to be overcome for electron transfer, reflecting the energy requirements of electron transport in the membrane^{34,35}. The results in Fig. 2d, e show the values of E_a for CNTs-PVDF membranes are in the range of between 0.0038 eV for CNTs-PVDF₁₀₀ and 0.011 eV for CNTs-PVDF₃₀, while the values for CNTs-PAN and CNTs-PES membranes are as high as 0.31 eV and 0.46 eV, respectively. The E_a value of CNTs-PVDF membrane is far lower than those of CNTs-PAN and CNTs-PES membranes, implying that electrons could transfer from one CNT to other CNTs through β -phase PVDF chains much more easily than through PAN or PES polymer chains. With an increase in temperature, more electrons could

acquire enough energy to overcome energy barrier and transfer from one CNT to another, which is the reason that the conductivity of CNTs-PVDF₁₀₀ membranes increases with increasing temperature. The good electrical conductivity of CNTs-PVDF membranes may be attributed to the strong dipole interactions between β -phase PVDF chains and CNTs surfaces, which facilitates local charge redistribution through overlapping dipole moments from β -PVDF and delocalized π -electrons from CNTs, establishing pathways for efficient electron transport (Fig. 2f), which needs further exploration.

The mass ratio of CNTs to PVDF could also affect the electrical conductivity of CNTs-PVDF membranes. Experimental results show that, with the increase of the mass ratio of CNTs to PVDF from 0.2 to 0.5, the electrical conductivity of resultant CNTs-PVDF membranes increases correspondingly from 18.2 to 94.5 S m⁻¹ (Supplementary Fig. 21). The result is predictable because more CNTs in the CNTs-PVDF membranes could provide more conductive paths. However, when the mass ratio exceeds 0.3, as shown in Supplementary Fig. 22, the mechanical strength of the prepared CNTs-PVDF membranes deteriorated, indicating an unstable structure. Therefore, the membranes prepared at a high mass ratio of CNTs to PVDF are not further discussed in this study.

Narrow pore size distribution is an important characteristic of high-quality membranes, which could endow the membranes with high selectivity and antifouling performance. By using CNTs-PVDF₈₅ membrane as an example, we analyze the pore size distribution of CNTs-PVDF membranes. As shown in Fig. 3a, the pore size distribution curve of CNTs-PVDF₈₅ membranes shows that more than 99% of their pores are distributed within the range between 51 and 57 nm, with a sharp peak at 52 nm. Comparatively, four commercially obtained PVDF membranes from internationally renowned brands with a similar pore size of around 50 nm (named as CM1, CM2, CM3, and CM4, respectively) have much wider pore size distributions. Quantitative analysis indicates that the pore size distributions span 6 nm (51–57 nm) for CNTs-PVDF₈₅ membranes, which is narrower than 32 nm (51–83 nm) for CM1, 20 nm (45–65 nm) for CM2, 10 nm (45–55 nm) for CM3, and 8 nm (38–46 nm) for CM4, respectively. The narrower pore size distribution of CNTs-PVDF membranes may be attributed to the interwoven CNTs framework in membranes restricting the formation of irregular and oversized pores during phase inversion. The narrow pore size distribution could help the CNTs-PVDF membranes achieve more precise separation and higher antifouling performance than commercial PVDF membranes.

Permeance of CNTs-PVDF membranes and antifouling performance by electrifying

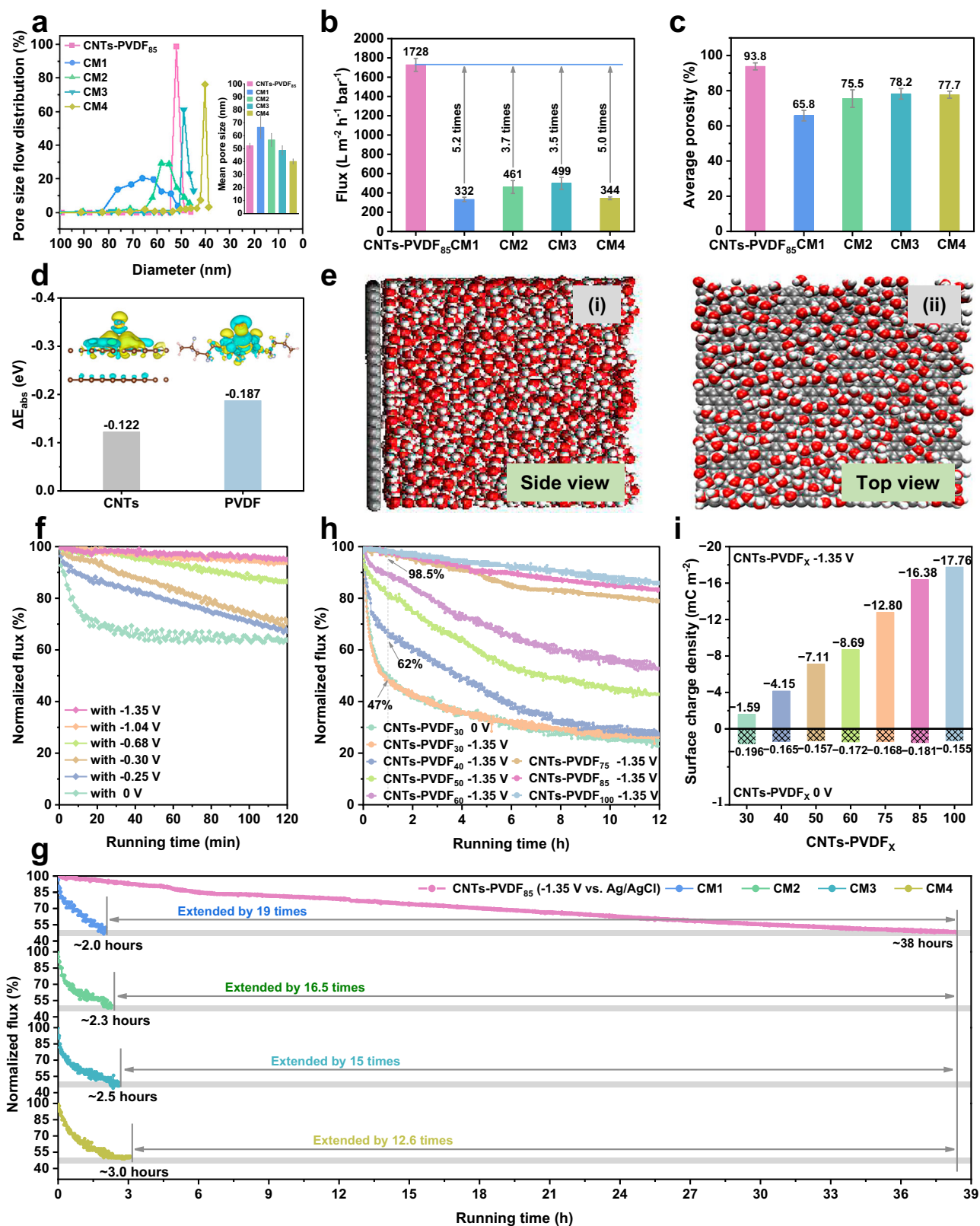
The CNTs-PVDF₈₅ membrane is selected for evaluation of performance of the ECMs from the perspective of balancing water permeance, mechanical strength and electrical conductivity (Supplementary Figs. 13 and 23). The experimental results show that the CNTs-PVDF₈₅ membrane has a high water permeance of 1728 L m⁻² h⁻¹ bar⁻¹, which is 3.5–5.2 times as much as those of three commercially obtained PVDF membranes with a similar pore size of around 50 nm as shown in Fig. 3b (specifically, 5.2 times, 3.7 times, and 3.5 times as much as those of CM1, CM2, and CM3, respectively). The water permeance for CM4 is measured to be 209 L m⁻² h⁻¹ bar⁻¹. We could not compare the water permeances of the CNTs-PVDF₈₅ directly to that of CM4 because it has 12 nm smaller pore size than CNTs-PVDF₈₅. We could not directly compare the water permeance of CNTs-PVDF₈₅ with CM4 due to the 12 nm smaller average pore size of CM4 (~40 nm vs. 52 nm for CNTs-PVDF₈₅). Assuming CM4 had equivalent 52 nm pore size as CNTs-PVDF₈₅ membrane, its permeance could be estimated to be 344 L m⁻² h⁻¹ bar⁻¹. It means that CNTs-PVDF₈₅ membrane exhibits about 5.0-fold higher permeance than CM4 with similar pore size. To investigate the reason for the excellent permeance of CNTs-PVDF membranes, their porosity was measured (Fig. 3c). It was found that

the CNTs-PVDF₈₅ membranes have a high porosity of 93.8%, which is higher than those (65.8%–78.2%) of commercial PVDF membranes, suggesting that the CNTs-PVDF₈₅ membranes possess more channels for water transport. According to the Hagen–Poiseuille equation, the membrane permeability is proportional to its porosity; therefore, the permeance of CNTs-PVDF₈₅ membranes should be theoretically 1.2–1.4 times as much as those of PVDF membranes, which is much lower than the actual permeance increase of 3.5–5.2 times observed. It suggests that the increase of porosity is not the main reason for obviously high permeance of CNTs-PVDF₈₅, there must be other reason that plays more important role in obvious permeance augment.

Benefitting from the interactions between CNTs and β -phase PVDF, the pristine CNTs without any surface modification could be well dispersed into organic solvents. As a result, their atomically smooth and hydrophobic surface is retained in CNTs-PVDF membranes. The first-principle calculation shows that the adsorption energy of -0.122 eV between pristine CNTs and water molecules is significantly lower than that between PVDF and water molecules (-0.187 eV), suggesting that water molecules could undergo a much lower transport resistance in CNTs-based membranes than in PVDF membranes (Fig. 3d). Molecular dynamics (MD) simulations reveals that there exists a vacuum gap between water molecules and the surface of CNTs (Fig. 3e). The vacuum gap could minimize the water-wall friction between water molecules and CNTs, allowing a free-slip flow in CNTs-based membranes. As revealed, because of minimized hydrogen bond interactions between oxygen-containing functional groups and water molecules, the pristine CNTs are conducive to ultrafast transport of water molecules at water-CNTs interface, which could be the main reason for ultrahigh permeance of CNTs-PVDF membranes. The comprehensive comparison between CNTs-PVDF₈₅ and commercial PVDF membranes suggests that CNTs-PVDF membranes could be outstanding for practical applications.

Membrane fouling is one of the great challenges facing current membrane-based separation technologies, which could result in a serious flux decline and an obvious operating cost increase. NOM is one of the major reasons for membrane fouling during drinking water treatment³⁶. Therefore, humic acids, the most common component in NOM and inherently negatively charged in surface water, are used to investigate the antifouling performance of CNTs-PVDF membranes. The CNTs-PVDF₈₅ membrane with conductivity of 51.2 S m⁻¹ is chosen and an electrified membrane process, equipped with CNTs-PVDF₈₅ membrane is constructed for evaluation of antifouling performance under electrifying condition. The CNTs-PVDF₈₅ membrane is used as working electrode, and a tubular titanium mesh positioned coaxially outside the membrane was applied as the non-reactive counter electrode. (Supplementary Figs. 24 and 25 and Table 4). The membrane system was connected with electric power system for potential supply and regulation (Supplementary Fig. 26). The electro-regulation is realized by applying a negative potential to the membranes, which is tuned by external voltage. As the external voltage increases from 0 to 3 V, the potentials on the membranes change from 0 to -1.35 V (Supplementary Fig. 27a). The corresponding potentials on titanium mesh change from 0 to +1.65 V vs Ag/AgCl, which is far lower than the required potential for passivation by forming an insulating TiO₂ layer. Cyclic voltammetry (CV) analysis reveals the absence of reduction peaks in the corresponding CV curves in the potential range, suggesting no detectable hydrogen evolution reaction occurs within the applied potential range (Supplementary Fig. 27b). The results demonstrate that the electrified membrane process consumes little energy.

As shown in Fig. 3f, without applying an external potential, the flux of CNTs-PVDF₈₅ membranes decreased to 67% of the initial flux after a 1-h treatment of water with 10 mg L⁻¹ HA, indicating HA could cause membrane fouling. When a low potential of -0.3 V vs. Ag/AgCl was applied on the membrane, the flux decline could be obviously



retarded, as evidenced by a higher flux (88% of the initial flux) after a 1-h treatment. With an increase of the membrane potential from -0.3 V to -1.35 V vs. Ag/AgCl, their antifouling performance could be further improved. Specifically, at a potential of -1.35 V vs. Ag/AgCl, exhibiting excellent antifouling performance with only a 5% water flux decrease after 2-h treatment. After a prolonged operation time of 5 h, the CNTs-PVDF₈₅

membrane could preserve a high normalized flux of 90% at a potential of -1.35 V vs. Ag/AgCl. In contrast, the normalized flux of four commercial PVDF membranes (namely CM1, CM2, CM3, and CM4) decreased down to 30%–40% of their initial values (Supplementary Fig. 28). Further test showed that the flux of CNTs-PVDF₈₅ membranes was still above 50% of their initial value even after an operation of 38 h at a potential of -1.35 V vs. Ag/AgCl. By contrast, the fluxes of

Fig. 3 | Membrane performance evaluation. **a** Pore distribution of CNTs-PVDF, CM1, CM2, CM3 and CM4 membranes. Inserted image is the mean pore size. **b** Comparison of pure water permeances of CNTs-PVDF, CM1, CM2, CM3 and CM4 membranes (CM1, CM2, CM3 and CM4 are commercial PVDF membranes from internationally renowned brands). **c** Average porosity of CNTs-PVDF, CM1, CM2, CM3 and CM4 membranes calculated according to the Griess method. **d** DFT-calculated adsorption energies of CNTs-water and β -PVDF-water. Inserted images are DFT-calculated electron density difference distributions between CNTs/water and PVDF/water, respectively. **e** MD-calculated water molecular adsorption

behavior at CNTs-water interface. **f** Normalized flux decreasing of CNTs-PVDF membrane filtrating HA solution under external potentials of 0 V, -0.25 V, -0.30 V, -0.68 V, -1.04 V, -1.35 V vs. Ag/AgCl. **g** Backwash intervals of the CNTs-PVDF membrane were extended by 12.6-19 times longer than those of the CM1, CM2, CM3, and CM4 membranes. **h** Antifouling performance comparison of CNTs-PVDF membranes under external potential of -1.35 V vs. Ag/AgCl. The dashed line is guide to the eye. **i** Surface charge density of CNTs-PVDF membranes under external potentials of 0 V and -1.35 V vs. Ag/AgCl. Error bars indicate the standard deviations from three different samples. The data are presented as mean \pm SD.

commercial PVDF membranes declined by 50% within only 2–3 h (around 2.0 h for CM1, 2.3 h for CM2, 2.5 h for CM3, and 3.0 h for CM4) under the same pressure difference of 0.5 bar. The results indicate that the electrically conductive CNTs-PVDF membranes have an extraordinarily high antifouling capability under electrifying conditions. The backwash cycle of the CNTs-PVDF₈₅ membrane was extended to 12.6–19 times as long as those of four commercial PVDF membranes (Fig. 3g). Consequently, benefited from the high water permeance and the prolonged backwash cycle of CNTs-PVDF membrane, the membrane material cost and the energy cost for the production of 1 m³ of water in bench-scale could be saved by 66% and 76% in comparison to commercial PVDF membrane, respectively. (Supplementary Fig. 29 and Tables 5 and 6). The antifouling performance of CNTs-PVDF₈₅ membrane was further evaluated by bovine serum albumin (BSA) and sodium alginate (SA), which represent protein substances and polysaccharide substances, respectively. The results show that the CNTs-PVDF₈₅ membrane can prolong backwash cycle by 6.4–21.3 times and 7.5–9.7 times, respectively (Supplementary Figs. 30 and 31). These results demonstrated the universality of the electrostatic repulsion antifouling mechanism against negatively charged contaminants in drinking water sources.

In order to explore the critical role of electric conductivity of membrane materials in antifouling performance, we measured the flux decline by using the membrane with different electrical conductivity under a certain potential supply. As shown in Fig. 3h, when the CNTs-PVDF membranes were used as the cathode under an applied potential of -1.35 ± 0.03 V, the water flux decline was suppressed, correlating with the enhanced conductivity of the membrane. Specifically, the flux of CNTs-PVDF₃₀ membrane with a conductivity of 3.6 S m⁻¹ decreased by about 53% and 75% of its initial value after 1-h and 12-h operation (Supplementary Fig. 32). For CNTs-PVDF₄₀ membrane with a conductivity of 6.9 S m⁻¹, the flux decreased by about 38% and 70% of its initial value after 1-h and 12-h operation. For CNTs-PVDF₅₀, CNTs-PVDF₆₀, and CNTs-PVDF₇₅ membranes with conductivity of 12.8, 17.7, and 29.3 S m⁻¹, the flux declined by 20%, 9%, and 3% after 1-h operation, and 53%, 47%, and 21% after 12-h operation, respectively. When the conductivity increased to 51.2 S m⁻¹ and further to 64.0 S m⁻¹ as the case of CNTs-PVDF₈₅ and CNTs-PVDF₁₀₀, we observed almost no flux decline after 1-h operation, and only 17% and 14% flux decline after 12-h operation. Moreover, the effects of voltage drop along the membrane were investigated. As shown in Supplementary Figs. 33 and 34, the voltage drop was only 0.86 V at a distance of 25 cm and the antifouling performance was similar to that at the energized point of external voltage, where the membrane pores remained clearly visible with rare attachment of foulants. The voltage drop would increase to 1.36 V at a distance of 50 cm and 2.15 V at 100 cm, which would indeed diminish the electrochemical effects. Subsequent research will be continuously conducted to show that the problem could be readily resolved by establishing 3–4 electrical contact points at equal intervals along the axial direction of the membranes. The results above indicate that the ECMs could reveal excellent antifouling performance under electrifying condition, which suggests that, benefiting from the electrical conductivity of CNTs-PVDF membranes, applying negative potential to the CNTs-PVDF membranes could inhibit adherence of negatively

charged humic acids on membranes surfaces, thereby mitigating membrane fouling.

To understand the mechanism underlying the electrochemically improved antifouling performance, the surface charge densities of as-prepared membranes were measured. As shown in Fig. 3i, when the CNTs-PVDF membranes were used as the cathode, the negative potential on them could greatly increase their surface charge. For example, the surface charge density of CNTs-PVDF₁₀₀ membranes was significantly increased from 0.155 mC m⁻² at 0 V to 17.8 mC m⁻² under a potential of -1.35 V. Moreover, with an increase in electric conductivity from 3.6 to 64.0 S m⁻¹, the surface charge density correspondingly increased from 1.6 mC m⁻² for CNTs-PVDF₃₀ membranes to 17.8 mC m⁻² for CNTs-PVDF₁₀₀ membrane. Due to negatively charged nature of HA in natural water (for example, the zeta potential of 10 mg L⁻¹ HA solution is measured to be -45.5 mV), the increased surface charge density of CNTs-PVDF membranes induced by increased potential applied could enhance the electrostatic repulsion between membrane surface and HA molecules, which could be one of major reasons to the improved antifouling performance of CNTs-PVDF membranes under negative electrifying (Fig. 4a). Density functional theory (DFT) calculations indicate that the adsorption energy (ΔE_{ads}) between CNTs and HA molecule is -34.2 Kcal mol⁻¹, suggesting HA molecules are able to be adsorbed on CNTs (Fig. 4b–d). When a negative potential is applied on the CNTs with a charge density of $2e^-$ nm⁻², the ΔE_{ads} become $+15.6$ Kcal mol⁻¹, suggesting that HA molecules are prone to be detached from CNTs. Both the calculation and experimental results well support the electrostatic repulsion mechanism for significant improvement of antifouling performance, which assumes the electrostatic repulsion between membrane surfaces and HA molecules could obviously alleviate membrane fouling. To verify the universality of the antifouling strategy to other fouling contaminants, we measured zeta potentials of other common fouling substances in water, such as sodium alginate, BSA, oleic acid (representing vegetable oil), n-hexadecane (representing mineral oil), and bentonite colloids. As shown in Supplementary Table 7, the zeta potentials of all these substances are negatively charged when they exist in pure water at ppm level, implying that electrostatic repulsion mechanism realized by applying negative potential to ECMs could be universal strategy for antifouling against various foulants.

To further investigate the antifouling mechanism, the surface free energies of CNTs-PVDF₈₅ membrane and four commercial PVDF membranes are measured. As shown in Supplementary Fig. 35, the CNTs-PVDF₈₅ membrane has a high surface free energy of 55.9 mN m⁻¹, which is obviously higher than those of commercial PVDF membranes (46.9 mN m⁻¹ for CM1, 41.1 mN m⁻¹ for CM2, 48.1 mN m⁻¹ for CM3, 43.7 mN m⁻¹ for CM4). The high surface free energy of CNTs-PVDF₈₅ is attributed to their polarized β -phase PVDF characterized by an all-trans planar zigzag conformation with polar $-CF_2-CF_2$ dipoles aligned in the same direction. It is also found when -1.35 V potential is applied to the membranes by applying 3.0 V voltage, the surface free energy of CNTs-PVDF₈₅ membrane is increased to 57.1 mN m⁻¹. Higher value of surface free energy means that water interacts more strongly with the membrane, leading to the membrane to be more hydrophilic (Supplementary Fig. 36). MD simulations show that there exists a dense water

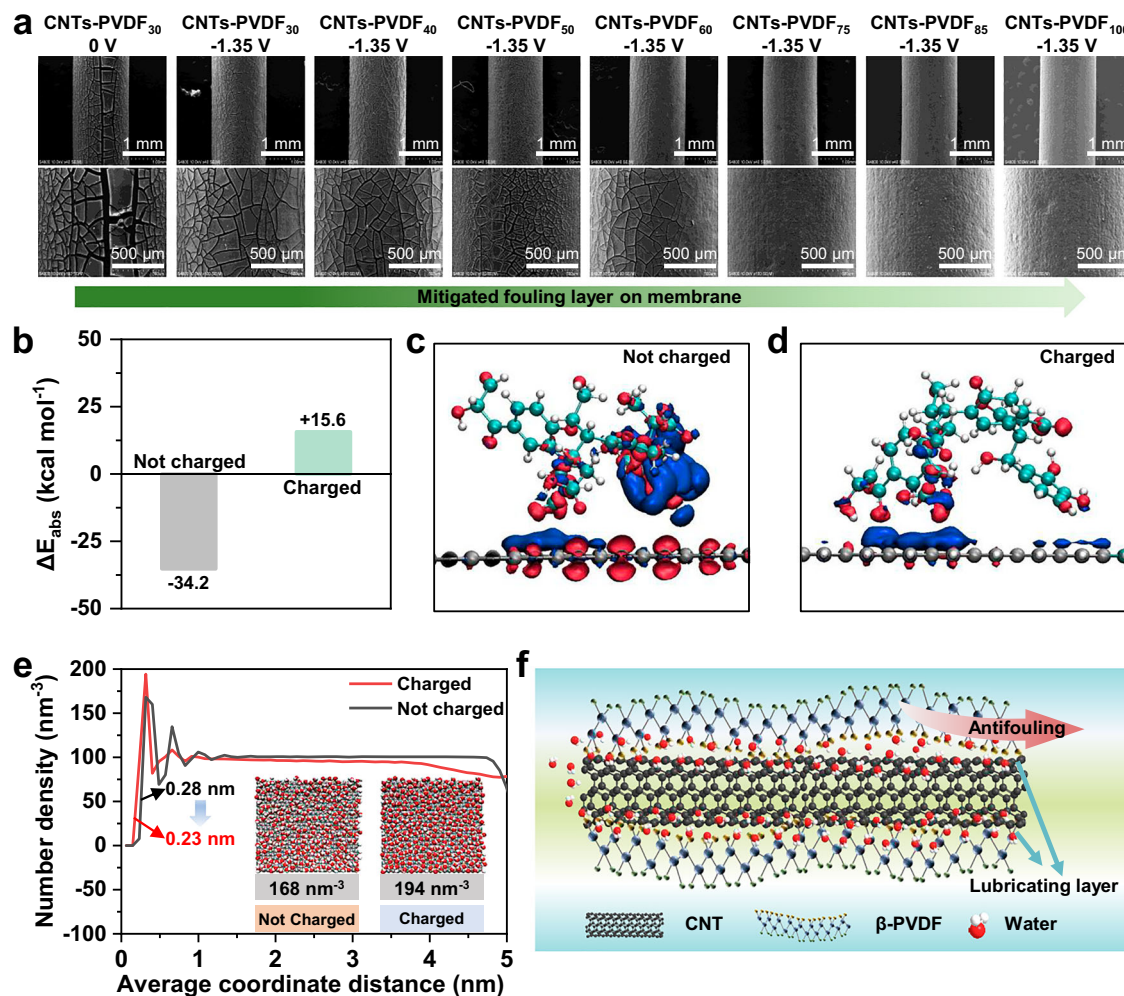


Fig. 4 | Mechanisms of antifouling behavior by CNTs-PVDF membrane. **a** SEM images of fouled surface of CNTs-PVDF₃₀, CNTs-PVDF₄₀, CNTs-PVDF₅₀, CNTs-PVDF₆₀, CNTs-PVDF₇₅, CNTs-PVDF₈₅, CNTs-PVDF₁₀₀ membranes. **b** DFT-calculated adsorption energies between HA and membrane under external potential of 0 V and -1.35 V vs. Ag/AgCl. **c**, **d** MD simulation of water molecules aside CNTs in the

CNTs-PVDF membrane with or without external electrical potential. **e** DFT-calculated water molecule distribution and density near the CNTs in the CNTs-PVDF membrane. Inserted images are MD-calculated water molecular adsorption behavior at CNTs-water interface. **f** Schematic of ordered water molecules aside the CNTs-PVDF membrane that enhances antifouling.

layer at water/CNTs interface with a water molecule density of 168 nm^{-3} , which is increased to 194 nm^{-3} in the water layer when the CNTs have a charge density of $2e^- \text{ nm}^{-2}$ (Fig. 4e). Moreover, the water molecules are more ordered and closer to the CNTs. The dense water layer could create a shielding effect that prevents the direct physical attachment of foulants onto the membrane surface (Fig. 4f). The results demonstrate that both electrostatic repulsion and dense water layer are responsible for the excellent antifouling performance of CNTs-PVDF membranes under electrifying conditions.

Flux recovery efficiency by back washing is an important indicator that reflects the anti-irreversible fouling ability of membranes. It was observed that when no potential was applied during water treatment, the flux recovery of CNTs-PVDF₈₅ membranes was 70% after three filtration-backwash cycles (Supplementary Figs. 37 and 38), which is higher than that of commercial CM1 (58%), CM2 (30%), CM3 (50%), and CM4 (64%) membranes. The results suggest the CNTs-PVDF₈₅ membrane possessed intrinsic capability for anti-irreversible fouling. When a potential of -1.35 V vs. Ag/AgCl is applied to the CNTs-PVDF₈₅ membranes during filtration process, the flux recovery by back-washing could reach to nearly 100% (Supplementary Fig. 39), which is much higher than those of all commercial membranes tested (30%–64%) under the same conditions. To evaluate the leaching risk of CNTs from the membranes, the effluents during filtration,

backwashing and chemical cleaning processes were collected at 20, 40, and 60 min, and were then filtered through a blank PVDF substrate membrane. The SEM images of the membranes confirmed the absence of CNTs in effluent (Supplementary Figs. S40–S43), which evidences that no CNTs were detached from the membranes during filtration, backwashing, and chemical-cleaning processes. Given the time limitations, allowing only a short run of the experiment, the result would be further confirmed in subsequent work via a longer-term evaluation ranging from several months to even years. The results indicate that the negative potential applying could effectively suppress the formation of irreversible fouling during water treatment (Supplementary Fig. 44).

Demonstration for scalable production of CNTs-PVDF ECMs

In order to demonstrate the feasibility of scalable production of the CNTs-PVDF hollow fiber ECMs, we performed a demonstration project in a membrane production plant in Tianjin, China. We adopt a continuous wet-spinning process with a production rate of $11.5 \text{ m}^2 \text{ h}^{-1}$ (corresponding to an annual yield of $100,000 \text{ m}^2$). The operating parameters of the wet-spinning process were directly adopted from laboratory experiments (Fig. 5a and Supplementary Fig. 45). The parameters, which characterize membrane quality, such as water permeance, electric conductivity, structural strength, porosity, and

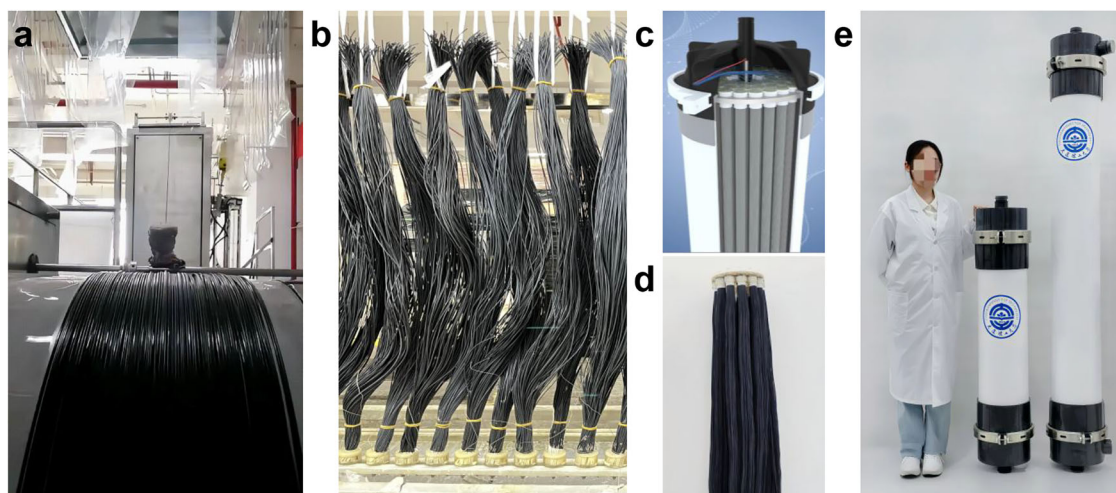


Fig. 5 | Scalable fabrication of CNTs-PVDF membrane. **a** The real-time fabricated CNTs-PVDF membrane in the production line. **b** CNTs-PVDF membrane bundles for the assembly of membrane modules. **c, d** Schematic diagram and a digital image of a commercial scale membrane module based on CNTs-PVDF. Containing

membrane bundles, titanium mesh counter electrode, and the connecting wires hollow fiber membranes. **e** Digital images of the circular membrane modules. The typical sizes of the modules are $\Phi \times L = 238 \text{ mm} \times 1200 \text{ mm}$ and $\Phi \times L = 238 \text{ mm} \times 2000 \text{ mm}$, respectively.

water contact angle of produced CNTs-PVDF ECMs are summarized in (Supplementary Fig. 46). As revealed, the main parameters of the CNTs-PVDF ECMs produced by full-scale process are similar to those prepared in lab-scale, indicating that the magnification of production scale retains the high performance of CNTs-PVDF ECMs. The cost of CNTs-PVDF ECMs production, mainly from raw materials including CNTs, PVDF, pore-forming agents, and solvents (Supplementary Tables 8–10), is determined to be about $\$2.1 \text{ m}^{-2}$, which is comparable to those of commercial PVDF membranes. Their high performance, feasibility of scalable production, and low cost endow the CNTs-PVDF ECMs with great potential to be practically applied as advanced new-generation membranes.

The membrane modules applying for electrified process were designed, in which the electrically conductive membrane fibers were fixed together in a bundle, and connected to a titanium wire using both conductive adhesive and epoxy resin (Fig. 5b, c). A tubular titanium mesh was used as the counter electrode and placed on the inner wall of the modules (Fig. 5d). The membrane modules could be customized on demand with various sizes and conformations. For example, Fig. 5e shows two commercial-scale column-type membrane modules, which have different lengths of 1200 mm and 2000 mm with the same outer diameter of 238 mm.

Field demonstration for drinking water treatment applying electrified membrane process equipped with ECMs

Decentralized water purification solution is critical in underdeveloped areas lacking robust infrastructure or in secondary water supply for urban communities. The essential facilities for this purpose must be characterized by effective removal of pathogens and suspended particulates, easily deployable designs, minimal energy requirement and maintenance, and modular scalability. Herein, a field demonstration is performed for evaluation of performance of the electrified membrane process equipped with ECMs in water treatment. Membrane filtration equipment was constructed by utilizing twenty membrane modules, equipped with CNTs-PVDF ultra-filtration ECMs with average pore size of 15 nm and electric conductivity of 45 S m^{-1} . The total effective membrane area of the equipment is 125 m^2 (Fig. 6a), providing a water production capacity of $300 \text{ m}^3 \text{ day}^{-1}$. According to UN recommendations, the daily per capita water consumption is 50–100 L in undeveloped regions and 150–300 L in urban areas, respectively³. Thus, this field demonstration could meet the water demands of 3000–6000

people in low-income villages or 1000–2000 people in urban communities. The demonstration was performed in a drinking water treatment plant Dalian, China. The plant adopts a conventional water treatment process of coagulation/sedimentation, sand filtration, and chlorination. The raw water is from a reservoir nearby. As illustrated in Supplementary Fig. 47, the water treatment process was consisted of a pre-treatment unit with a polypropylene cotton filter followed by the electrified membrane filtration unit with -0.92 V potential on the membranes by applying 2.0 V voltage.

Figure 6b, c show the daily water production yield and monitored trans-membrane pressure difference during a 100-day running, respectively. As revealed, the engineering demonstration runs smoothly in a constant-flow mode with a daily water treatment capacity of 300 m^3 . As shown in Fig. 6c, the transmembrane pressure difference of the CNTs-PVDF membranes increased by 2 times after around 5-h treatment, which suggests that the membrane flux decreased by 50% during this period. As recommended in *Dow Water & Process Solutions* and practical engineering experience^{37–39}, a backwash is generally required when the membrane flux declines by 50%. Thus, the engineering demonstration reveals a backwash cycle of 5 h for the CNTs-PVDF ECMs. In comparison, the flux of conventional ultrafiltration membranes usually decreases to about 50% of initial value within 0.5 h, as reported in previous studies on membrane-based water treatment processes^{37–41}. The results evidence that the backwashing interval for the CNTs-PVDF ECMs could be significantly extended by about 10 times as much as those of the conventional membranes.

The routine monitoring of water quality shows that the turbidity in effluent of the electrified membrane process was 0.1 NTU, which was much better than that in effluent (1.1 NTU) from the drinking water treatment plant by conventional process (Fig. 6d and Supplementary Figs. 48 and 49). Meanwhile, the electrified membrane process could reduce total organic carbon (TOC) from 3.9 mg L^{-1} in feed to 2.8 mg L^{-1} in effluent, while TOC in effluent of conventional process is 3.6 mg L^{-1} (Fig. 6e) with only slight TOC removal. As evidenced by a third-party water quality examination (Supplementary Fig. 50), the quality of effluent from the electrified membrane process meets the requirements of China's Drinking Water Sanitation Standards (GB5749-2022) with 97 water quality indicators. Especially, the electrified membrane process could remove pathogenic bacteria, such as *Escherichia coli*, with 100% complete removal from 360 MPN/100 mL to 0 MPN/100 mL without feeding any chemical disinfectant to the water, indicating the

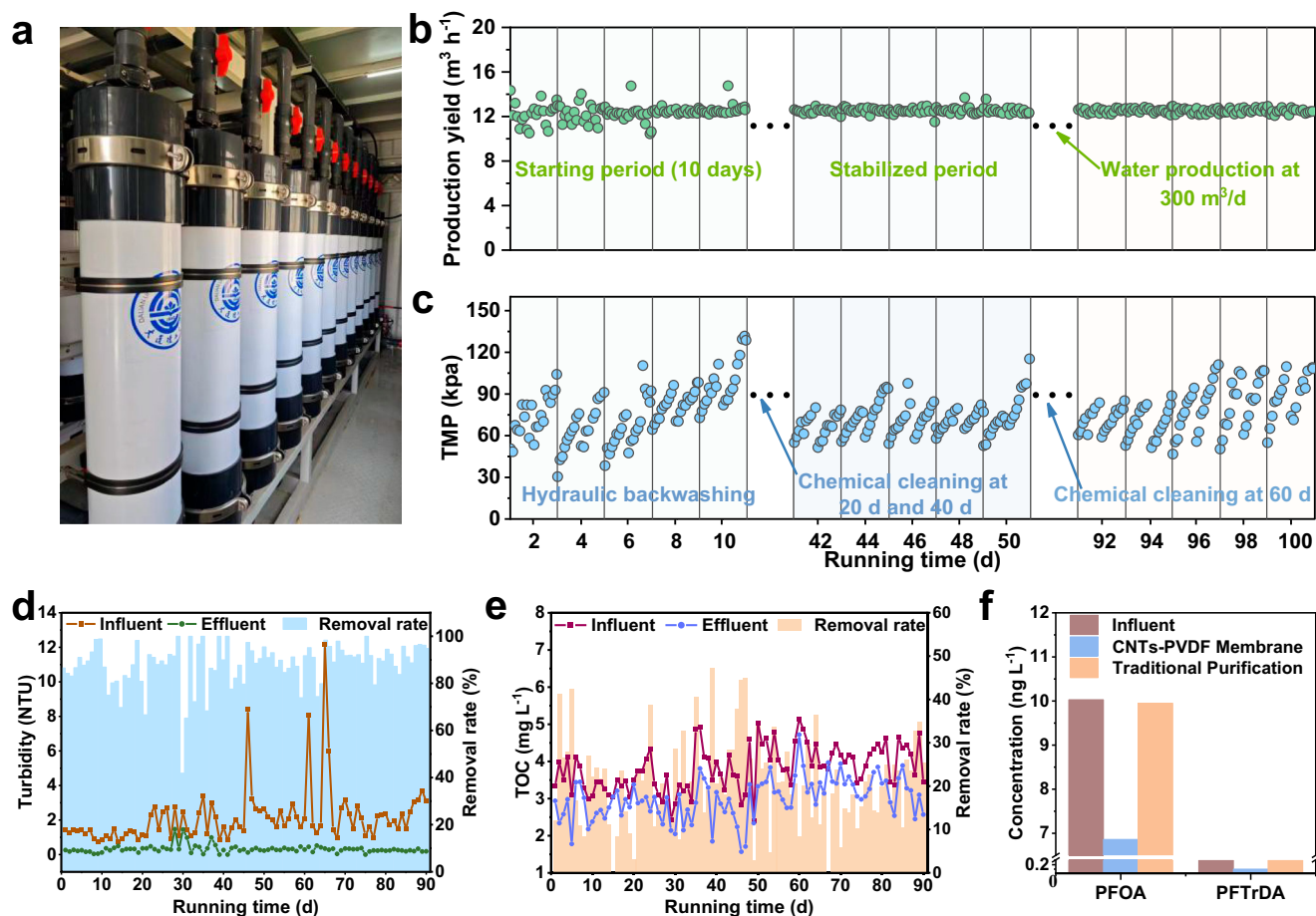


Fig. 6 | Field demonstration of CNTs-PVDF membrane for drinking water treatment. **a** Assembled membrane modules for the engineering demonstration (20 columns). **b, c** Monitoring chart of daily water production yield (designed being $300 \text{ m}^3 \text{ d}^{-1}$) and transmembrane pressure curves for 100 days at constant-flow

mode. **d, e** Monitoring of turbidity, TOC, and removal efficiency for the membrane effluent. **f** Comparison for the removal capabilities of PFOA and PFTrDA by CNTs-PVDF membrane and coagulation-sedimentation-sand filtration process in water treatment plant.

demonstration process is more environmentally friendly than conventional water treatment process (Supplementary Fig. 51). Usually, microbiological indicators such as pathogens are regarded as the most critical parameters for drinking water safety in underdeveloped regions (up to thousands of MPN L^{-1} in contaminated source water)³⁷, which often lack adequate sanitation and rapidly outbreaks of water-borne diseases including diarrhea, cholera, and typhoid fever. Thus, the complete removal of pathogens by ECMs could ensure the safety of drinking water especially in undeveloped areas. Moreover, the electrified membrane process possesses the capability for removal of trace emerging organic pollutants. For example, the process could remove perfluorooctanoic acid (PFOA) and perfluorotridecanoic acid (PFTrDA) (detected from the influent water with their concentrations of 10 ng L^{-1} and 0.3 ng L^{-1} respectively) with removal efficiency of 32% and 66% respectively (Fig. 6f). In contrast, the concentrations of PFOA and PFTrDA in the effluent keep almost same to those of influent by conventional process. Both PFOA and PFTrDA have a negatively charged group of $-\text{COO}^-$ due to the deprotonation of the carboxyl group at neutral pH in natural surface water⁴². These negatively charged carboxylate groups could be electrostatically repulsed by negatively electrified CNTs-PVDF membranes. Meanwhile, some portion of them could be adsorbed onto the surfaces of natural colloids and NOMs^{43,44} due to the hydrophobic nature of perfluorinated chain of PFOA and PFTrDA, and rejected by the CNTs-PVDF membranes.

In addition to removal of contaminants, low energy requirement is also critical for sustainable drinking water provision in

underdeveloped areas. Benefited from the excellent antifouling performance of CNTs-PVDF ECMs, their cost for chemical cleaning was decreased from \$11.52 per kiloton water for commercial PVDF membranes to \$0.55 (Supplementary Table 11), saving about 95% cost. Meanwhile, the energy consumption of the electrified membrane process was recorded to be 0.05 kWh m^{-3} , which is only about 45% that for commercial PVDF membranes (0.11 kWh m^{-3}) (Supplementary Table 12). Based on such low energy requirements, for the water demands of 3000 - 6000 people in a village of an underdeveloped region, for example, in Africa, the daily electricity consumption for the ECMs water treatment equipment could be easily satisfied by a photovoltaic device with a total area of 30–60 m^2 under their superior sunlight conditions³⁹. The results indicate that the electrified CNTs-PVDF membrane process demonstrates huge advantages over conventional water treatment processes, showing substantial application potential in underdeveloped regions. Moreover, due to the low maintenance and energy requirements with better water quality, the ECMs-based electrified processes are also applicable to secondary water supply demands in urban communities.

We proposed a strategy of assembling CNTs into in-situ phase-converted polarized PVDF to produce electrically conductive CNTs-PVDF membranes with high water permeance and high mechanical strength concurrently. Their water permeance is 3.5 - 5.2 times as high as those of commercial PVDF membranes from internationally renowned brands with a similar pore size because of the intrinsic atomically smooth and hydrophobic surface, and their high porosity

and thin separation layer. The CNTs-PVDF membranes exhibit a good electrical conductivity, which is sufficient for reaching the aim for regulating membrane surface charges, and thus promoting membrane performance. As a result, the CNTs-PVDF ECMs show excellent anti-fouling performance under electrifying conditions owing to electrostatic repulsion and the dense water layer on membrane surface induced by electrowetting, with a backwash cycle more than ten times as long as those of commercial PVDF membranes. The production of the CNTs-PVDF membranes in an actual production line with a capacity of $11.5 \text{ m}^2 \text{ h}^{-1}$ demonstrates the feasibility of the industrial-scale production of the membranes. The field demonstration for drinking water treatment with a capacity of $300 \text{ m}^3 \text{ d}^{-1}$ verifies that the electrified membrane process equipped with the CNTs-PVDF ECMs is much more energy-efficient and cost-effective than conventional membrane processes, and produces drinking water with much better quality in terms of turbidity, TOC, pathogen, and certain trace emerging contaminants compared with conventional water treatment process. This work offers an innovative strategy to improve markedly membrane performance for water treatment and could advance our understanding for the mechanisms of the electrified membrane process underlying the application of ECMs, which could promote the advances in membrane technology in the field of drinking water treatment and related fields. Such an innovative membrane technology is preferably matched with decentralized water supply systems serving for dozens to thousands of people in underdeveloped regions by presenting a safe, cost-effective, and easily managed solution, fostering substantial improvements in public health and driving sustainable development.

Methods

Materials and reagents

The CNTs (array tube GT-401, outer diameter: 10–20 nm, length: 50–100 μm) powder was obtained from Nanchang Yifeng Nano Materials Co., Ltd, China. PVDF (FR904W) powder was purchased from Inner Mongolia Sanai Fu Wanhao Fluorochemical Co., Ltd, China. N-N-Dimethylacetamide (DMAC, AR, $\geq 99\%$), polyvinylpyrrolidone K30 (PVP K30, GR, $\geq 99\%$), polyethylene glycol 400 (PEG 400, AR, $\geq 99\%$), and glycerol (AR, $\geq 99\%$) were purchased from Tianjin Kemiou Chemical Reagent Co., Ltd, China. All chemicals and reagents were of analytical grade and used without further purification.

Preparation of CNTs-PVDF membrane and module

The CNTs-PVDF membrane was fabricated by a method of wet-spinning followed by phase conversion. $1020 \times \text{g}$ of DMAC was added into a stainless-steel reactor and stirred at low speed. The aligned CNTs, polyvinylpyrrolidone K30 (PVP K30), and polyethylene glycol 400 (PEG 400) were gradually added, maintaining a mass ratio of $m_{\text{CNTs}}: m_{\text{PVP}}: m_{\text{PEG 400}}$ at 1:3:1. The mixture was composed of $50 \times \text{g}$ of CNTs, $150 \times \text{g}$ of PVP-K30, and $50 \times \text{g}$ of PEG-400. The mixture was stirred continuously for 12 h to achieve homogeneous dispersion. Subsequently, the reactor heating temperature was set in stages from ambient temperature to 40°C – 60°C . Next, PVDF ($150 \times \text{g}$) was added into the dispersion, maintaining a mass ratio of CNTs: PVDF at 1:3. The solution was further heated and stirred for 12 h until the PVDF was fully dissolved. Finally, the casting solution was degassed under vacuum to eliminate the dissolved air. For the fabrication process, compressed air was introduced into the reactor to pressurize and discharge the spinning dope until no visible air bubbles were observed in the discharge stream, and then the spinneret was installed. The spinning solution was employed as the shell fluid, and a 70% DMAC aqueous solution was used as the core fluid. The rotation speeds of the spinning metering pump and core fluid metering pump were adjusted to control the shell and core fluid flow rates at a predefined ratio (optimal at 85:15). The solution was extruded into a 60°C water coagulation bath and then wound onto a winding roller. Upon completion of spinning, the membrane bundles on the winding roller were taken down and then

immersed in high-purity water to remove residual organic solvents and pore-forming agents. Subsequently, the washed membranes were placed into a 70°C water bath and kept for 1–2 h, followed by immersing in a 30% glycerol aqueous solution for 12 h. After the membrane fibers were hung to air-dry naturally, we obtained the final CNTs-PVDF membrane products.

The membrane module assembly consists of a cylindrical pressure-resistant outer shell, counter electrodes, insulating layer, CNTs-PVDF membranes, and water collection fittings. The counter electrodes are fixed along the inner wall of the shell and at the central axis of the module. An insulating layer is positioned between the counter electrodes and the CNTs-PVDF hollow fiber membranes. Bundles of hollow fiber membranes are sealed at the inlet and outlet ports. At the inlet side, one end of each hollow fiber is sequentially sealed with epoxy resin, conductive adhesive, and another layer of epoxy resin. Electrical wires connected to the composite CNTs-PVDF hollow fiber membranes and those linked to the counter electrodes are routed through side ports and connected to an external DC regulated power supply.

Characterization of membrane structures and properties

The morphology of the membranes was examined using a field-emission scanning electron microscope (Hitachi S-4800, Japan). The tensile tests were performed by a Universal material testing machine (SHIMADZU Autograph AGS-X, 100 N, Japan). An X-ray diffractometer (XRD, D8 ADVANCE, Bruker, Germany) was utilized to determine the phase structure. The 2D-WAXD patterns were recorded on a Rigaku Ultima IV (Rigaku, Tokyo, Japan) with Cu K α radiation ($\lambda = 1.5405 \text{ \AA}$). To analyze the chemical composition and structural properties, a Fourier transform infrared spectrometer (FTIR, Thermo Fisher Scientific Nicolet iS20, USA) was employed. Elemental content was assessed using an energy-dispersive X-ray spectrometer (XPS, Thermo Scientific, UK) equipped with an Al K α X-ray source. The water and diiodomethane contact angles of the membranes were measured with an optical contact angle and interfacial tension meter (SL200KB, KINO Industry Co. Ltd.). For each liquid, three independent measurements with $\sim 2 \mu\text{L}$ droplets were performed on each membrane; detailed descriptions of the contact angle measurement procedures are provided in the Supporting Information. The pore size distributions of the CNTs-PVDF and commercial PVDF membranes were analyzed by the Capillary Flow Porometer (POROLUX 1000, IB-FT GmbH, Berlin, Germany). Prior to measurement, membrane samples (3 cm in length) were subjected to a solvent exchange process by sequential immersion in ethanol-water mixtures and then dried in oven at 30°C . The dried samples were sealed in a sample holder using epoxy resin, with one end closed off. The measurements were conducted using Porefil as the wetting liquid (surface tension: 16 dynes cm^{-1}) and nitrogen as the purge gas. The pore size distribution was calculated by the instrument software based on the standard capillary flow principle. The porosity of the CNTs-PVDF and commercial PVDF membranes were obtained by means of dry-wet weighting method. The electro-conductivity of the CNC-HFMs was obtained from a four-point probe meter (RTS-8; 4 Probes Tech, Guangzhou, China). The Zeta potentials of the contaminant solution was measured by a Zeta potential analyzer (Zetasizer Nano ZS 90, England). The Zeta potential of the membranes were determined using a SurPASS electrokinetic analyzer (Anton Paar surpass3, Austria); Zeta potential measurements were performed in 0.1 mM KCl solution at pH 7.0 and 25°C ; the reported values represent the mean of three independent measurements. The open circuit potential-time bias potential curves (under external voltage of 0, 1.0, 1.5, 2.0, 2.5, and 3.0 V), EIS, and CV (potential range: -0.25 V to -2 V vs. Ag/AgCl) were recorded using an electrochemical workstation (Chenhua CHI660D). The CNTs-PVDF hollow fiber membrane was employed directly as the working electrode, with a tube diameter of 1.5 mm, length of 2 cm, and carbon nanotube loading of 25%.

The turbidity of water samples was measured in nephelometric turbidity units (NTU) using a turbidimeter (LP2000-11, Hanna Instruments, Italy). The instrument was calibrated with a series of Formazin standard solutions (0.1, 1, 10, and 100 NTU) after establishing a baseline with turbidity-free water. Prior to measurement, samples were homogenized by gentle inversion and analyzed in a cuvette pre-rinsed with the sample.

TOC was determined on an Analytikjena TOC analyzer (multi N/C@2100, Germany). Water samples were filtered through a 0.45 µm membrane filter prior to analysis. The measurements were conducted by high-temperature catalytic combustion, with an injection volume of 0.2 mL.

The concentrations of PFAS were quantified using ultra-performance liquid chromatography coupled with triple quadrupole mass spectrometry. Chromatographic separation was performed on an Agilent 1200SL UPLC system equipped with an Eclipse Plus C18 column (2.1 × 100 mm, 3.5 µm) maintained at 40 °C. The mobile phase consisted of 10 mM ammonium acetate in water (A) and methanol (B), delivered at a flow rate of 0.25 mL min⁻¹ with the following gradient program: 40% B (0–3 min), increased linearly to 90% B (3–20 min), then to 100% B (20–30 min), and held at 100% B for 3 min (30–33 min). Mass spectrometric detection was carried out on an Agilent 6410B triple quadrupole instrument operated in negative electrospray ionization mode. The capillary voltage was set at 4.0 kV, with a desolvation gas temperature of 350 °C and a flow rate of 8.0 L min⁻¹.

Total coliforms and *Escherichia coli* in water samples were detected and quantified using the 10-tube enzyme substrate method in strict accordance with the Chinese National Standard GB/T5750.12-2006. A comprehensive description of the analytical procedure is provided in the Supporting Information.

Evaluation of membrane performance

The performance tests of pressure-driven membrane filtration processes were conducted using a constant-pressure cross-flow filtration setup. The feed solutions were compressed into the membrane module and a constant transmembrane pressure of 0.5 bar was maintained by a regulating valve. The membrane was pressurized for one hour before each performance test. The pure water permeance (P_w , L m⁻² h⁻¹ bar⁻¹) and the organic matter rejection rate (R , %) were calculated by the following equations:

$$P_w = \frac{\Delta V}{A \times \Delta t \times \Delta P} \quad (1)$$

$$R = \left(1 - \frac{C_p}{C_f}\right) \times 100\% \quad (2)$$

where ΔV is the volume of penetrant solution, A is the effective membrane area, Δt is the filtration time, ΔP is the transmembrane pressure difference, and C_p and C_f are the concentrations of organic matter in the permeate and feed, respectively.

The integrated water treatment process in field demonstration comprises prefiltration and membrane filtration. Pretreatment was carried out using a 20 µm polypropylene (PP) filter to remove large particulate matter such as sediment and colloids. The subsequent electrically conductive CNTs-PVDF membrane filtration effectively removed bacteria, viruses, NOM, biomacromolecules, nano/micro-scale colloids. The system operated automatically under constant-flow mode with a backwashing interval of 5 h. In the electro-assisted membrane filtration unit, a voltage of 2.0 V was applied with the membrane serving as the cathode. Chemical cleaning was initiated when the transmembrane pressure (TMP) increased by approximately 0.1 MPa as the initial TMP value could not be restored by backwashing.

The chemical cleaning procedure employed a 2000 ppm sodium hypochlorite solution.

DFT Calculations and MD Simulations

All first-principles calculations are performed using the plane-wave projector-augmented wave method, as implemented in the Vienna ab initio simulation package (VASP5.4.4)⁴⁵. The Perdew–Burke–Ernzerhof form of generalized gradient approximation is chosen as the exchange–correlation potential⁴⁶. Grimme’s DFT-D3(BJ) method was used to describe the vdW interaction. The energy cutoff of 520 eV was used for structural relaxation. k-spacing was set to 0.4 for all structures to allow the smallest spacing between k-points in the unit of 0.4 Å⁻¹. The conjugated gradient method is utilized to optimize the geometry with the convergence threshold of 10⁻⁵ eV in energy and 0.01 eV/Å in force, respectively.

The adsorption energy E_{ads} is calculated as:

$$E_{ads} = E_{tot} - E_{PVDF/C} - E_{H_2O} \quad (3)$$

Where E_{tot} is the total energy of PVDF or graphene after adsorption of H₂O, $E_{PVDF/C}$ is the energy of the PVDF or graphene, and E_{H_2O} is the energy of a single H₂O molecule. DFT calculations were performed using the Gaussian 16 program package⁴⁷. All the DFT computations were performed by the B3LYP density functional method with the D3GJ dispersion correction⁴⁸.

All the MD simulations were carried out by GROMACS software package. The no-charged and charged (2e/nm²) graphene sheet have an area of 5.1 × 5.1 nm². The SPC/E model was used for the water molecules. A time step of 1 fs was employed, and all chemical bonds connecting hydrogen atoms were constrained using LINCS algorithm. A cut-off radius of 15.0 Å with the nearest image convention was used for the van der Waals interaction calculations. Electrostatic interactions were evaluated by particle mesh Ewald method with a direct space cut-off distance of 15.0 Å. After energy minimization, a 10 ns NVT simulation was performed, the trajectories of the last 2 ns are used for analysis. The computational model and results could be found in Supplementary Data 1.

Statistics and reproducibility

All experiments were repeated three times replicates. The data are presented as mean ± standard deviation (SD) from three replicates. No statistical method was used to predetermine sample size. No data were excluded from the analyses; the experiments were not randomized; the investigators were not blinded to allocation during experiments and outcome assessment.

Data availability

All data supporting the findings of this study are available in the main text, Methods, Supplementary Information or source data files. Source data are provided with this paper.

References

- Barbier, E. *The Water Paradox: Overcoming the Global Crisis in Water Management* (Yale University Press, 2019).
- Peters, T. Membrane technology for water treatment. *Chem. Eng. Technol.* **33**, 1233–1240 (2010).
- Malik, A. et al. Polarizing and equalizing trends in international trade and sustainable development goals. *Nat. Sustain.* **7**, 1359–1370 (2024).
- Greve, P. et al. Global assessment of water challenges under uncertainty in water scarcity projections. *Nat. Sustain.* **1**, 486–494 (2018).
- Shannon, M. A. et al. Science and technology for water purification in the coming decades. *Nature* **452**, 301–310 (2008).

6. Fane, A. G., Wang, R. & Hu, M. X. Synthetic membranes for water purification: status and future. *Angew. Chem. -Int. Ed.* **54**, 3368–3386 (2015).
7. Gong, W., Bai, L. & Liang, H. Membrane-based technologies for removing emerging contaminants in urban water systems: limitations, successes, and future improvements. *Desalination* **590**, 117974 (2024).
8. Van der Bruggen, B., Vandecasteele, C., Van Gestel, T., Doyen, W. & Leysen, R. A review of pressure-driven membrane processes in wastewater treatment and drinking water production. *Environ. Prog.* **22**, 46–56 (2003).
9. Zhang, Y. et al. Piezoelectric polyvinylidene fluoride membranes with self-powered and electrified antifouling performance in pressure-driven ultrafiltration processes. *Environ. Sci. Technol.* **56**, 16271–16280 (2022).
10. Zhao, Y. et al. Pulsed hydraulic-pressure-responsive self-cleaning membrane. *Nature* **608**, 69–73 (2022).
11. Sun, J. et al. Maintaining antibacterial activity against biofouling using a quaternary ammonium membrane coupling with electro-repulsion. *Environ. Sci. Technol.* **57**, 1520–1528 (2023).
12. Wei, G. et al. Constructing all carbon nanotube hollow fiber membranes with improved performance in separation and antifouling for water treatment. *Environ. Sci. Technol.* **48**, 8062–8068 (2014).
13. Zhang, H. et al. Electrostatic-induced ion-confined partitioning in graphene nanolaminate membrane for breaking anion-cation co-transport to enhance desalination. *Nat. Commun.* **15**, 4324 (2024).
14. Kang, Y. et al. Unveiling the spatially confined oxidation processes in reactive electrochemical membranes. *Nat. Commun.* **14**, 6590 (2023).
15. Lee, B. et al. A carbon nanotube wall membrane for water treatment. *Nat. Commun.* **6**, 7109 (2015).
16. Hinds, B. J. et al. Aligned multiwalled carbon nanotube membranes. *Science* **303**, 62–65 (2004).
17. Yang, H. Y. et al. Carbon nanotube membranes with ultrahigh specific adsorption capacity for water desalination and purification. *Nat. Commun.* **4**, 2220 (2013).
18. Zhang, Z. et al. Mitigation of irreversible membrane biofouling by CNTs-PVDF conductive composite membrane. *Environ. Res.* **267**, 120703 (2025).
19. Gao, G., Zhang, Q. & Vecitis, C. D. CNT–PVDF composite flow-through electrode for single-pass sequential reduction–oxidation. *J. Mater. Chem. A* **2**, 6185–6190 (2014).
20. Zhang, Q. & Vecitis, C. D. Conductive CNT-PVDF membrane for capacitive organic fouling reduction. *J. Membr. Sci.* **459**, 143–156 (2014).
21. Zhang, Z., Hu, W., Ma, C., Zhang, T. & Wang, L. Mitigation of irreversible membrane fouling by CNT-PVDF electrically conductive ultrafiltration membranes. *J. Water Process. Eng.* **67**, 106168 (2024).
22. Mavukkandy, M. O., Zaib, Q. & Arafat, H. A. CNT/PVP blend PVDF membranes for the removal of organic pollutants from simulated treated wastewater effluent. *J. Environ. Chem. Eng.* **6**, 6733–6740 (2018).
23. Zhou, R., Rana, D., Matsuura, T. & Lan, C. Q. Effects of multi-walled carbon nanotubes (MWCNTs) and integrated MWCNTs/SiO₂ nano-additives on PVDF polymeric membranes for vacuum membrane distillation. *Sep. Purif. Technol.* **217**, 154–163 (2019).
24. Zhang, X., Lang, W., Yan, X., Lou, Z. & Chen, X. Influences of the structure parameters of multi-walled carbon nanotubes(MWNTs) on PVDF/PFSA/O-MWNTs hollow fiber ultrafiltration membranes. *J. Membr. Sci.* **499**, 179–190 (2016).
25. Zhang, X. et al. Improved performances of PVDF/PFSA/O-MWNTs hollow fiber membranes and the synergism effects of two additives. *J. Membr. Sci.* **469**, 458–470 (2014).
26. Mandal, A. & Nandi, A. K. Ionic liquid integrated multiwalled carbon nanotube in a poly (vinylidene fluoride) matrix: formation of a piezoelectric β -polymorph with significant reinforcement and conductivity improvement. *ACS Appl. Mater. Interfaces* **5**, 747–760 (2013).
27. Yu, S. et al. Formation mechanism of β -phase in PVDF/CNT composite prepared by the sonication method. *Macromolecules* **42**, 8870–8874 (2009).
28. Ho, T. M., Razzaghi, A., Ramachandran, A. & Mikkonen, K. S. Emulsion characterization via microfluidic devices: a review on interfacial tension and stability to coalescence. *Adv. Colloid Interface Sci.* **299**, 102541 (2022).
29. Misaran, M. S., Sarbatly, R., Bono, A. & Rahman, M. M. Effect of extrusion rate on morphology of Kaolin/PolyEtherSulfone (PESf) membrane precursor. *IOP Conf. Ser.: Mater. Sci. Eng.* **160**, 12013 (2016).
30. Viswanath, P. & Yoshimura, M. Light-induced reversible phase transition in polyvinylidene fluoride-based nanocomposites. *SN Appl. Sci.* **1**, 1519 (2019).
31. Tashiro, K. et al. Electric-field-induced phase transition and crystal structural change of the oriented poly (vinylidene fluoride) β form as clarified by the in situ synchrotron wide-angle X-ray diffraction measurement. *Macromolecules* **55**, 6644–6660 (2022).
32. He, S., Guo, M., Wang, Y., Liang, Y. & Shen, Y. An optical/ferroelectric multiplexing multidimensional nonvolatile memory from ferroelectric polymer. *Adv. Mater.* **34**, 2202181 (2022).
33. Tian, B. B. et al. Tunnel electroresistance through organic ferroelectrics. *Nat. Commun.* **7**, 11502 (2016).
34. Xavier, P. F., Benoy, M. D., Stephen, S. K. & Varghese, T. Enhanced electrical properties of polyaniline carbon nanotube composites: analysis of temperature dependence of electrical conductivity using variable range hopping and fluctuation induced tunneling models. *J. Solid State Chem.* **300**, 122232 (2021).
35. Murdey, R., Katoh, K., Yamashita, M. & Sato, N. Thermally activated electrical conductivity of thin films of bis (phthalocyaninato) terbium (III) double decker complex. *Thin Solid Films* **646**, 17–20 (2018).
36. Xing, J. et al. Insight into Fe (II)/UV/chlorine pretreatment for reducing ultrafiltration (UF) membrane fouling: effects of different natural organic fractions and comparison with coagulation. *Water Res.* **167**, 115112 (2019).
37. Van der Bruggen, B., Lejon, L. & Vandecasteele, C. Reuse, treatment, and discharge of the concentrate of pressure-driven membrane processes. *Environ. Sci. Technol.* **37**, 3733–3738 (2003).
38. Li, Q. et al. Indirect evidence that colloidal deposition inside a hollow fiber ultrafiltration membrane exacerbated fouling during municipal wastewater reclamation. *ACS EST Eng.* **4**, 591–602 (2023).
39. Singh, R. *Membrane Technology and Engineering for Water Purification: Application, Systems Design and Operation* (Butterworth-Heinemann, 2014).
40. Remize, P. J., Guigui, C. & Cabassud, C. Evaluation of backwash efficiency, definition of remaining fouling and characterisation of its contribution in irreversible fouling: case of drinking water production by air-assisted ultra-filtration. *J. Membr. Sci.* **355**, 104–111 (2010).
41. Chang, H. et al. Hydraulic backwashing for low-pressure membranes in drinking water treatment: a review. *J. Membr. Sci.* **540**, 362–380 (2017).
42. Hubert, M., Meyn, T., Hansen, M. C., Hale, S. E. & Arp, H. P. H. Per- and polyfluoroalkyl substance (PFAS) removal from soil washing water by coagulation and flocculation. *Water Res.* **249**, 120888 (2024).
43. Richardson, S. D. & Ternes, T. A. Water analysis: emerging contaminants and current issues. *Anal. Chem.* **94**, 382–416 (2022).
44. Vu, C. T. & Wu, T. Recent progress in adsorptive removal of per- and poly-fluoroalkyl substances (PFAS) from water/wastewater. *Crit. Rev. Environ. Sci. Technol.* **52**, 90–129 (2022).

45. Kresse, G. & Furthmüller, J. Efficient iterative schemes for ab initio total-energy calculations using a plane-wave basis set. *Phys. Rev. B* **54**, 11169 (1996).
46. Perdew, J. P., Burke, K. & Ernzerhof, M. Generalized gradient approximation made simple. *Phys. Rev. Lett.* **77**, 3865 (1996).
47. Grimme, S., Antony, J., Ehrlich, S. & Krieg, H. A consistent and accurate ab initio parametrization of density functional dispersion correction (DFT-D) for the 94 elements H-Pu. *J. Chem. Phys.* **132**, 154104 (2010).
48. Grimme, S., Ehrlich, S. & Goerigk, L. Effect of the damping function in dispersion corrected density functional theory. *J. Comput. Chem.* **32**, 1456–1465 (2011).

Acknowledgements

This work was supported by the National Key Research and Development Program of China (2020YFA0211001) awarded to X.Q., the National Natural Science Foundation of China (52100074) awarded to J.J.X., the Programme of Introducing Talents of Discipline to Universities (B25041) awarded to X.Q., the Liaoning Province Science and Technology Planning Project (2022011918-JH25/101) awarded to X.Q., and the Fundamental Research Funds for the Central Universities (DUT2022TA04) awarded to J.J.X. The authors are grateful to Professor Wang Peng from Sun Yat-Sen University for a helpful discussion.

Author contributions

X.Q. and Y.K.Z. conceived the idea and designed the experiments. Y.K.Z., L.H.R., J.J.X., G.L.W., and H.D. synthesized the membranes. L.H.R., Y.K.Z., G.Z. H., H.D., and S.C. performed the membrane performance evaluations. J.J.X. and G.L.W. performed the computational calculations. X.Q., J.J.X., G.L.W., and Y.K.Z. co-wrote and revised the paper. X.Q. supervised the whole project. All authors have contributed to the discussion of the work.

Competing interests

The authors declare no competing interests.

Additional information

Supplementary information The online version contains supplementary material available at <https://doi.org/10.1038/s41467-025-66260-3>.

Correspondence and requests for materials should be addressed to Xie Quan.

Peer review information *Nature Communications* thanks Shuai Liang and the other, anonymous, reviewer(s) for their contribution to the peer review of this work. A peer review file is available.

Reprints and permissions information is available at <http://www.nature.com/reprints>

Publisher's note Springer Nature remains neutral with regard to jurisdictional claims in published maps and institutional affiliations.

Open Access This article is licensed under a Creative Commons Attribution-NonCommercial-NoDerivatives 4.0 International License, which permits any non-commercial use, sharing, distribution and reproduction in any medium or format, as long as you give appropriate credit to the original author(s) and the source, provide a link to the Creative Commons licence, and indicate if you modified the licensed material. You do not have permission under this licence to share adapted material derived from this article or parts of it. The images or other third party material in this article are included in the article's Creative Commons licence, unless indicated otherwise in a credit line to the material. If material is not included in the article's Creative Commons licence and your intended use is not permitted by statutory regulation or exceeds the permitted use, you will need to obtain permission directly from the copyright holder. To view a copy of this licence, visit <http://creativecommons.org/licenses/by-nc-nd/4.0/>.

© The Author(s) 2025